

Interspecies hydrogen transfer between cyanobacteria and symbiotic bacteria drives nitrogen loss

Received: 19 July 2024

Accepted: 20 May 2025

Published online: 31 May 2025

 Check for updatesLingrui Kong^{1,2}, Yiming Feng^{1,2}, Ru Zheng^{1,2}, Xiaogang Wu^{1,2}, Yimin Mao^{1,2},
Jingqi Sun^{1,2} & Sitong Liu^{1,2,3}  

The trace concentration of H₂ in most ecosystems after the Earth's oxidation has long caused the neglect of hydrogenotrophic denitrification for nitrogen loss. Here, we find that the interspecies hydrogen transfer between cyanobacteria and symbiotic bacteria within cyanobacterial aggregates is an undiscovered pathway for nitrogen loss. Cyanobacteria in aggregates can actively generate H₂ under the diel cycle as an electron donor for neighboring hydrogenotrophic denitrifiers. The hydrogenotrophic denitrification in engineered cyanobacterial aggregates accounts for a nitrogen removal rate of $3.47 \pm 0.42 \text{ mmol l}^{-1} \text{ day}^{-1}$. This value is nearly 50% of the heterotrophic denitrification rate, which far exceeds the general concept of the trace role. We find that H₂-evolving cyanobacteria and hydrogenotrophic denitrifiers coexist in 84% of the 63 globally distributed cyanobacterial aggregates, where bloom colonies and phototrophic mats from hot springs are identified as potential hotspots. We suggest that interspecies hydrogen transfer within cyanobacterial aggregates is possibly responsible for the excessive nitrogen loss rate during cyanobacterial blooms where cyanobacterial aggregates persist.

Molecular hydrogen (H₂) plays a crucial role as an electron and energy carrier in the microbial world. In the primordial stages of Earth, H₂ constituted a significant energy source available for life that comprised up to 30% of early Earth's air¹. The last universal common ancestor lived ~4.2 Ga ago and could harness energy from H₂². Although the atmospheric concentration of H₂ gradually became limited with the oxidation of the Earth¹, recent studies have revealed that the microbial capacity to aerobically oxidize trace H₂ for their growth is extensively distributed across marine and groundwater^{3,4}. Following oxygen, nitrate is the most energetically favorable electron acceptor⁵. Therefore, H₂ oxidation-driven denitrification may be an important microbial metabolism that impacts nitrogen cycling in an anaerobic environment. However, it is generally accepted that heterotrophic denitrification governs wide nitrogen loss⁶, and most modeling studies calculate the global denitrification rates using available carbon as an

electron donor^{7,8}. Hydrogenotrophic denitrification has long been overlooked, largely due to the trace H₂ concentration in most natural environments.

Interspecies hydrogen transfer (IHT) is a symbiotic metabolism where H₂ is transferred from H₂-producing microbes to hydrogenotrophic microbes⁹. Cyanobacteria, as prevalent primary producers, can produce H₂ through nitrogenase or bidirectional [NiFe] hydrogenase¹⁰, which primarily accounts for H₂ supersaturation in oceanic water¹¹. The high sensitivity of cyanobacterial hydrogenases or nitrogenase to oxygen generally limits their H₂ production in natural water, but the inhibition was reversible¹². In certain cases, some cyanobacteria can form aggregates, where the physical confinement limits oxygen diffusion and gives rise to H₂ production and IHT^{13–16}. For example, research on intertidal cyanobacterial mats has demonstrated that the H₂ production by cyanobacteria accounts for about 16% of the

¹College of Environmental Sciences and Engineering, Peking University, Beijing, PR China. ²Key Laboratory of Water and Sediment Sciences, Ministry of Education, Peking University, Beijing, PR China. ³Eco-environment and Resource Efficiency Research Laboratory, Shenzhen, PR China.

 e-mail: liusitong@pku.edu.cn

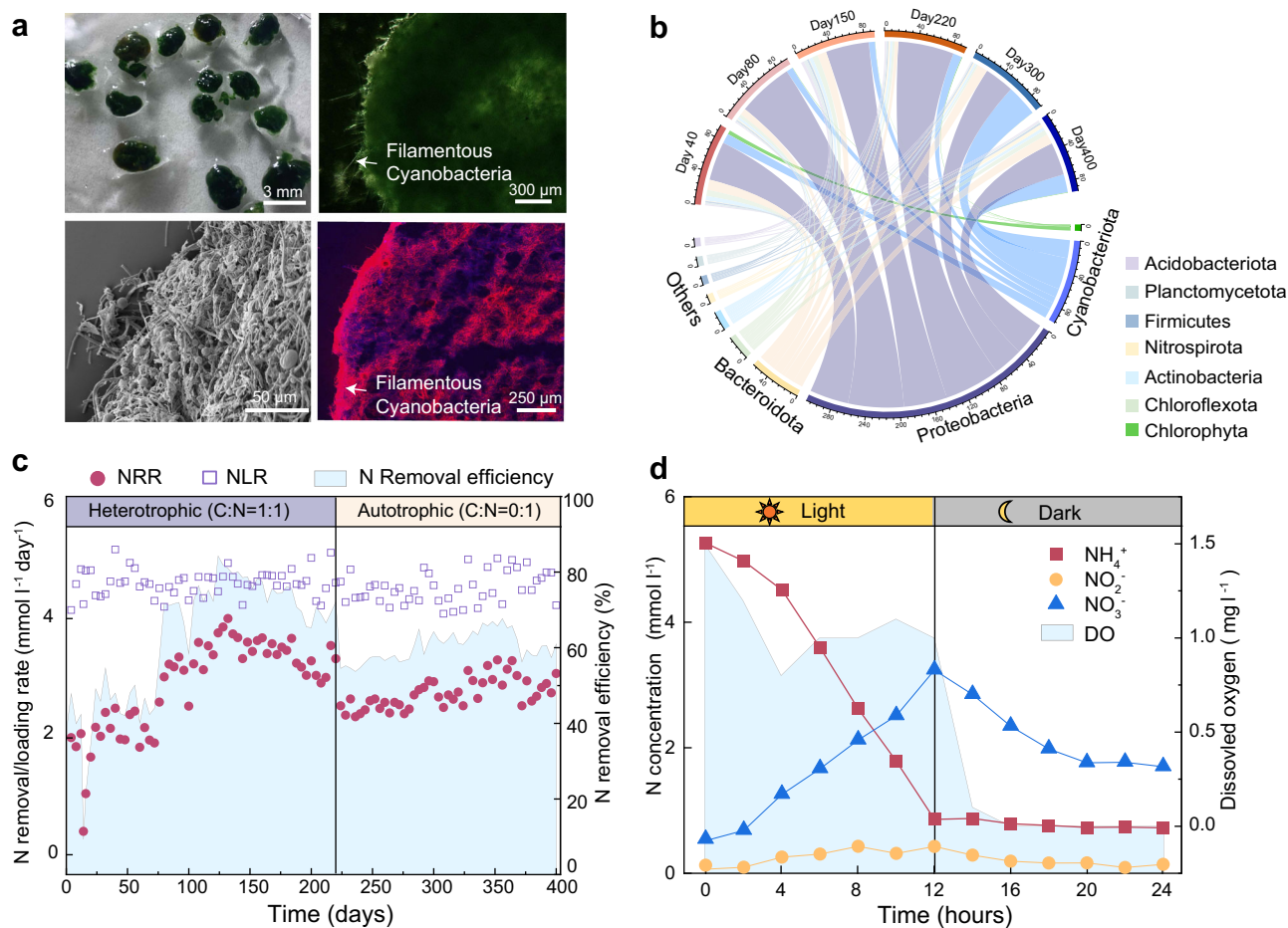


Fig. 1 | Morphology and nitrogen removal performance of engineered photogranules. **a** Morphology of photogranules according to microscopic observation, scanning electron microscopic observation, and CLSM images, the red signal represents the self-fluorescence of chlorophyll-a. Micrographs are representative results from 5 images. **b** Short-read based metagenomic microbial composition of photogranules at the phylum level. **c** Nitrogen removal performance of the photobioreactor during the 400-day operation. NLR: Nitrogen loading rate; NRR:

Nitrogen removal rate; The reactor initially was fed with acetate as the electron donor for denitrification, maintaining a low organic carbon-to-nitrogen (C: N) ratio of 1:1 during Days 0–220. The acetate was eliminated from the influent during Days 221–400 to make an autotrophic nitrogen removal system. **d** Nitrogen and dissolved oxygen (DO) profile of the photobioreactor in a typical cycle on Day 400. Source data are provided with this paper.

electrons fixed during photosynthesis¹⁶. Cyanobacterial aggregates (CA) are structured communities formed by the clustering of cyanobacteria and symbiotic bacteria. These aggregates are widely distributed across various ecosystems, including bloom colonies, phototrophic mats, glacier cryoconites¹⁷, and marine *Trichodesmium* colonies^{18,19}. Algal-bacterial interactions play an essential role in driving the biogeochemical cycle, and a recent study shows that the diatom-bacterium symbioses can contribute nearly half of the fixed nitrogen in the tropical North Atlantic²⁰. Currently, recognized cyanobacterial-bacterial IHT to date is primarily restricted to specific phototrophic mats with a focus on the sulfur and methane cycles^{21,22}. Notably, nitrate is prevalent in aquatic ecosystems, and nitrate reduction is energetically favored over sulfate reduction and methanogenesis in thermodynamics⁶. The high H_2 production potential, prevalence of nitrate, and close spatial matrix indicate a specialized niche for hydrogenotrophic denitrifiers in CA. Therefore, cyanobacterial-bacterial IHT may play a more active role in driving hydrogenotrophic denitrification.

Here, we show that IHT between cyanobacteria and symbiotic bacteria within cyanobacterial aggregates is an undiscovered pathway for nitrogen loss. To investigate IHT-driven denitrification in CA, we used photogranules²³, a type of engineered CA, as a controlled model system. We followed the aggregation process of cyanobacteria that

were exposed to diurnal cycles over a period of 400 days. In addition, we analyzed 63 metagenomes of globally distributed CA to demonstrate the universality of IHT-driven hydrogenotrophic denitrification. Our findings reveal that H_2 produced by cyanobacteria in CA during the diurnal cycle is an essential natural H_2 source to enrich the hydrogenotrophic denitrifiers. The IHT within CA unveils a previously unrecognized pathway for nitrogen loss in eutrophic aquatic ecosystems and may drive the evolution of early denitrifying microbes.

Results

Superior nitrogen loss rate of engineered CA without external electron donors

We cultivated photogranules in a photobioreactor that continuously operated for 400 days under a diurnal cycle (Supplementary Data 1). Filamentous cyanobacteria, which are the dominant photosynthetic phototrophic organisms, formed a thick edge and comprised a complex framework throughout the photogranules (Fig. 1a). Short-read based metagenomic analysis revealed that the microbial community in the photogranules harvested on the last operational day mainly consisted of Proteobacteria, Cyanobacteriota, Bacteroidota, and Chloroflexota at the phylum level. Chlorophyta, which was the only detected phylum of eukaryotic microalgae, accounted for <1% of the total microbial community (Fig. 1b).

The reactor finally achieved a superior nitrogen removal rate (NRR) of $3.5 \text{ mmol l}^{-1} \text{ day}^{-1}$ ($1.05 \text{ mg h}^{-1} \text{ g volatile suspended solid (VSS)}^{-1}$) without the addition of electron donors (Fig. 1c, Supplementary Fig. 1). This performance is nearly half of the heterotrophic NRR in engineered systems ($\sim 2.08 \text{ mg h}^{-1} \text{ gVSS}^{-1}$)²⁴. Nitrate mainly accumulated through nitrification during the light period and was removed during the dark period (Fig. 1d). Since no anammox bacteria were detected, the nitrogen removal in the photogranules system can primarily be attributed to assimilation and nitrification-denitrification. Batch tests with the addition of the nitrification inhibitor allylthiourea (ATU) demonstrated that microbial assimilation accounted for only $13.9 \pm 3.33\%$ of nitrogen removal (Supplementary Text 1, Supplementary Fig. 2), and denitrification was the main nitrogen removal pathway. Electron donors for denitrification are likely organic carbon and H_2 derived from nighttime cyanobacterial fermentation (Supplementary Text 2)²¹. Nevertheless, organic carbon was below the detection limit in the reactor effluent (Supplementary Fig. 1), and the addition of nighttime fermentative products improved the denitrification rate by only 13.4% (Supplementary Fig. 2). Therefore, we hypothesized that H_2 produced from cyanobacteria might act as an electron donor to drive the bacterial denitrification.

H_2 production and consumption pathways for nitrate reduction in CA

To test the hypothesis that H_2 drives denitrification, we determined the distribution of genes encoding hydrogenase via the functionally predictive classification scheme HydDB²⁵ from the 9 metagenomic samples (S1–S9), which were collected at different time points during the reactor operation (Fig. 2a). Overall, the gene abundance of total hydrogenase tended to increase with reactor operation, where multiple H_2 production and consumption pathways present (Fig. 2a). Accounting for >40% of the detected gene abundance of total hydrogenase (Supplementary Fig. 3), [NiFe] bidirectional (group 3) hydrogenase was the most dominant hydrogenase in the photogranules harvested on the last operational day. Most of these enzymes reversibly couple NAD(P)H oxidation to H_2 production and function as redox valves in anoxic conditions²⁵. Notably, [NiFe]–3d bidirectional hydrogenase in cyanobacteria works with a bias to H_2 production rather than H_2 oxidation²⁶. In contrast, other types of H_2 -evolving hydrogenases, such as [NiFe]-evolving (2%) and [FeFe]-evolving (4%), which are generally encoded by fermentative bacteria²⁵, were relatively rare. For H_2 uptake, [NiFe]-aerobic (14%) and [NiFe]-anaerobic uptake hydrogenases (16%) were evenly distributed (Supplementary Fig. 3). Notably, a significant positive correlation ($P < 0.001$, Spearman's $R > 0.7$) was observed among the gene abundances of dissimilatory nitrate reductases (*narG*), [NiFe]-bidirectional H_2 -hydrogenases and anaerobic uptake hydrogenases (Fig. 2b, c). In addition, the granular size appears to be a significant environmental factor that contributes to IHT, which was positively correlated ($P < 0.001$, Spearman's $R > 0.7$) with the three key genes (Fig. 2b). These correlation patterns indicated the presence of genes facilitating a coupled hydrogen cycle and hydrogenotrophic denitrification in the CA.

To determine which organisms are primarily responsible for the H_2 production and consumption, we analyzed the phylogenetic distribution and expression level of the hydrogenases of photogranules harvested on the last operational day across the high-quality MAGs. The rarefaction analysis indicated that the curves could approach saturation when samples from all time points were combined (Supplementary Fig. 4), suggesting sequence data covered most microbial species in the reactor. H_2 -evolving hydrogenases ([NiFe]-group 3, 4 and [FeFe]-groups A, B) had a relatively narrow distribution, where $\sim 95.4\%$ of transcripts (in terms of RPKM) were associated with [NiFe]–3d bidirectional hydrogenase of Cyanobacteria. Despite [FeFe]-hydrogenases being ultrafast for H_2 production, they were irreversibly inhibited to the O_2 produced by cyanobacteria^{12,25}. None of the

detected [FeFe] hydrogenases were expressed (Supplementary Fig. 5). This aligns with the observation in permeable sediments with oxic–anoxic transitions, where an extremely low abundance of [FeFe] hydrogenase and group 4 [NiFe]-hydrogenases was detected²⁷. To further substantiate that cyanobacteria produce H_2 , we isolated the most dominant H_2 -evolving cyanobacteria (*Pantanimema sp.*) from the photogranules²⁸ (Supplementary Text 3). Axenic *Pantanimema sp.* produced H_2 with an activity of $0.32 \pm 0.08 \mu\text{mol h}^{-1} \text{ mgVSS}^{-1}$ under dark anoxic conditions (Supplementary Fig. 6). H_2 -evolving cyanobacteria had a relatively high transcriptional abundance of 53% in the photogranules. Assuming a mass ratio of algae to be 3/8 in photogranules²⁹, it supported the high H_2 production activity of $0.17 \pm 0.12 \mu\text{mol h}^{-1} \text{ mgVSS}^{-1}$ of the photogranules (Supplementary Fig. 6). H_2 -evolving fermentative bacteria, which encoded [NiFe]-group-4 (0.16%) and [FeFe] hydrogenase (0.003%), had a relatively low transcriptional abundance. This is consistent with previous studies in which cyanobacterial fermentation mainly accounts for H_2 production in CA^{14,15,30}. Collectively, we demonstrated that cyanobacteria were the primary H_2 producers in photogranules, with some facultative bacteria potentially contributing a minor part.

In contrast, H_2 -uptake hydrogenases ([NiFe]-group 1, 2ade, 3) were phylogenetically widespread and encoded by nearly half (47%) of the bacterial MAGs (Fig. 2c). Group 1d, 2a, 2b [NiFe]-hydrogenases were the most widely distributed and highly expressed H_2 -uptake enzymes encoded in the metatranscriptome (Fig. 2c). These taxonomically widespread enzymes were all O_2 -tolerant and encoded by diverse facultative anaerobes²⁵. Most of those MAGs tended to increase with increasing reactor operation (Supplementary Fig. 7), which suggests a gradual enrichment of hydrogenotrophic bacteria. Among the H_2 -uptake hydrogenase-encoding MAGs, more than half also encoded the genes for nitrate reductases (*narG* and *napA*). These MAGs were predominantly affiliated with Burkholderiaceae and Rhodocyclaceae (Fig. 2d), which were previously shown to be facultative hydrogenotrophic denitrifiers in H_2 -supplied nitrogen removal bioreactors^{31,32}. Other hydrogenotrophic MAGs without nitrate reductases were mostly affiliated with Bacteroidota, Chloroflexota, and Myxococcota. These bacteria may be capable of using oxygen or sulfate as electron acceptors for H_2 oxidation to gain energy³ (Fig. 2d). By integrating the genomic information with the nitrogen removal profile, the H_2 production and utilization likely support diverse lifestyles and facilitate the nitrate reduction in photogranules.

Active H_2 production of cyanobacteria in the CA

To verify the metagenomic pathways responsible for H_2 metabolism, we employed a combination of tungsten oxide (WO_3) color change, gas chromatography, and microsensor measurements to explore the H_2 production characteristics of photogranules harvested at the end of reactor operation. WO_3 powder is commonly used as an indicator of H_2 production, which is suggested by a color change from light yellow to blue-gray³³. Here, WO_3 powder was added to the culture of photogranules under three conditions: continuous light, continuous dark, and a diurnal cycle. A discernible color change in WO_3 was observed only under diurnal cycling conditions after 48 h (Fig. 3a) with no color change under continuous light or darkness conditions (Fig. 3b, c). We subsequently monitored the amounts of H_2 in the headspace of the sealed anaerobic vial containing 0.19 gVSS photogranules by gas chromatography in a diurnal cycle. (Fig. 3d). When nitrate was supplied, H_2 was only detectable in the initial 4 h in the dark, followed by net consumption as darkness persisted (Fig. 3d). The nitrate assimilation, which is an intercellular electron sink, reduces the fermentative H_2 production of cyanobacteria³⁴. Since NH_4^+ is a reduced nitrogen source and typically prioritized by most cyanobacteria³⁵, we tested whether the uptake of NH_4^+ -N would save electrons and increase the H_2 production. Consistent with this hypothesis, substituting all NH_4^+ -N with NO_3^- -N in the culture medium resulted in an over 4-fold increase

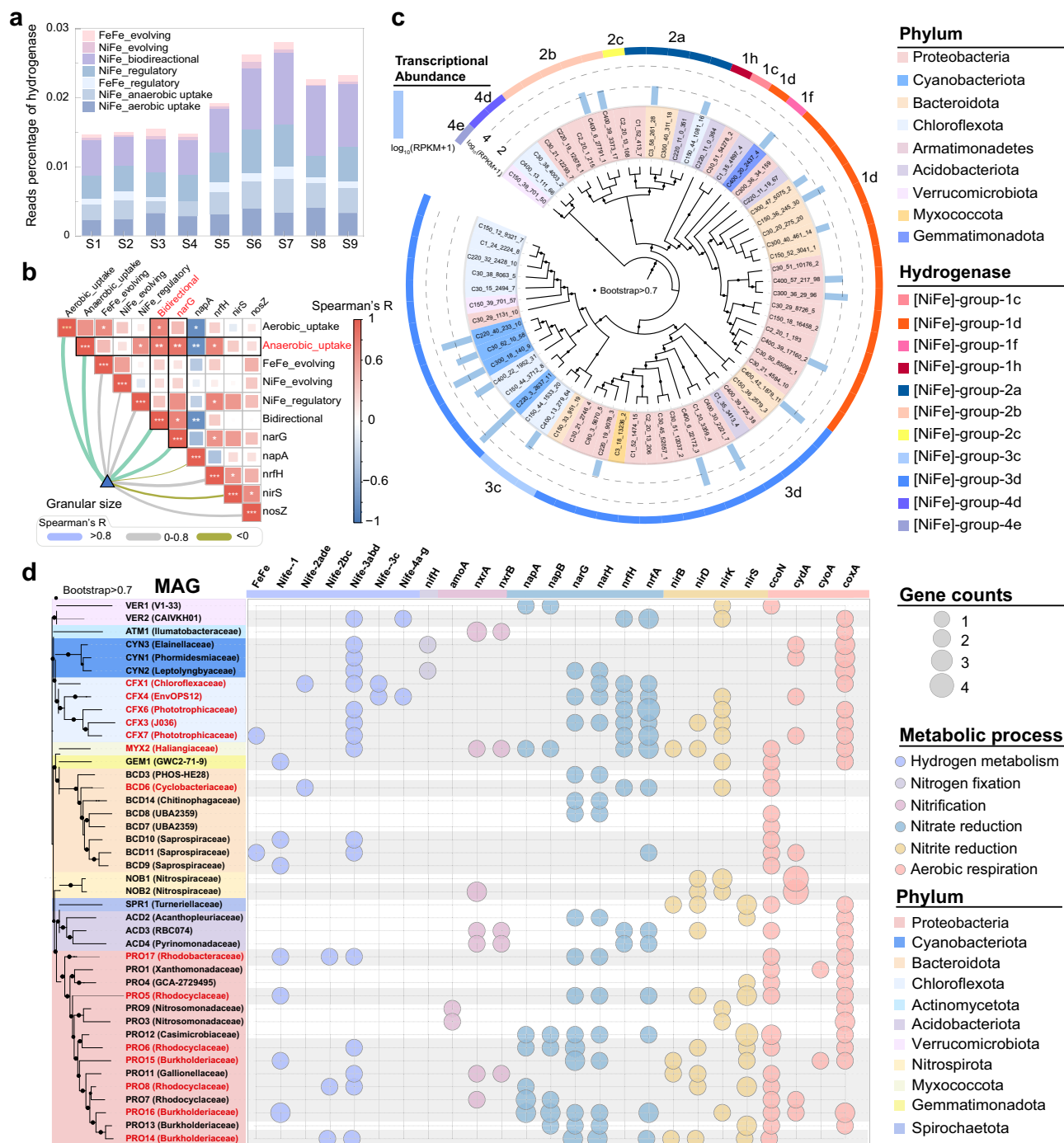


Fig. 2 | Distribution of metabolic genes encoded by photogranules' communities. **a** Functional classification and abundance of hydrogenase from the 9 metagenomic samples (S1–S9) collected in different time points (on Days 0, 20, 40, 60, 80, 150, 220, 300, 400, respectively) during reactor operation. No [Fe]-hydrogenases were detected in these metagenomes. Gene abundance was present in percentage of sequence reads for each hydrogenase type identified within one million random metagenome reads. **b** Spearman's correlation heatmap between hydrogenase gene abundance and denitrification gene abundance. Spearman's correlation coefficients are shown ($n = 9$ biologically independent samples). The asterisk indicates two-tailed test of Spearman's statistical significance adjusted. The significant correlations are indicated as follows: *, $P < 0.05$; **, $P < 0.01$; ***, $P < 0.001$. **c** Maximum-likelihood phylogenetic tree of the hydrogenase sequences retrieved from the high-quality MAGs (completeness >

90%, contamination < 10%) retrieved from the metagenomic samples of photogranules. Black circles indicate bootstrap support values over 70%. The transcriptional abundance of each hydrogenase sequence in the metatranscriptomic sample of photogranules (2–5 mm) harvested on day 400 was represented with $\log_{10}(\text{RPKM} + 1)$. **d** Bubble plot showing the metabolic potential of the 42 MAGs. Each MAG is noted as family level, and the right bar plot represents the relative abundance of MAGs in the photogranules harvested on the last operational day. The maximum likelihood phylogenetic tree of MAGs was constructed based on 37 marker gene families in the genome. The size of the circle corresponds to the number of functional genes in the specific MAGs, and marker genes that were not detected in any MAG are omitted. MAGs marked with red name represent the MAGs with hydrogenotrophic denitrification potential. Source data are provided with this paper.

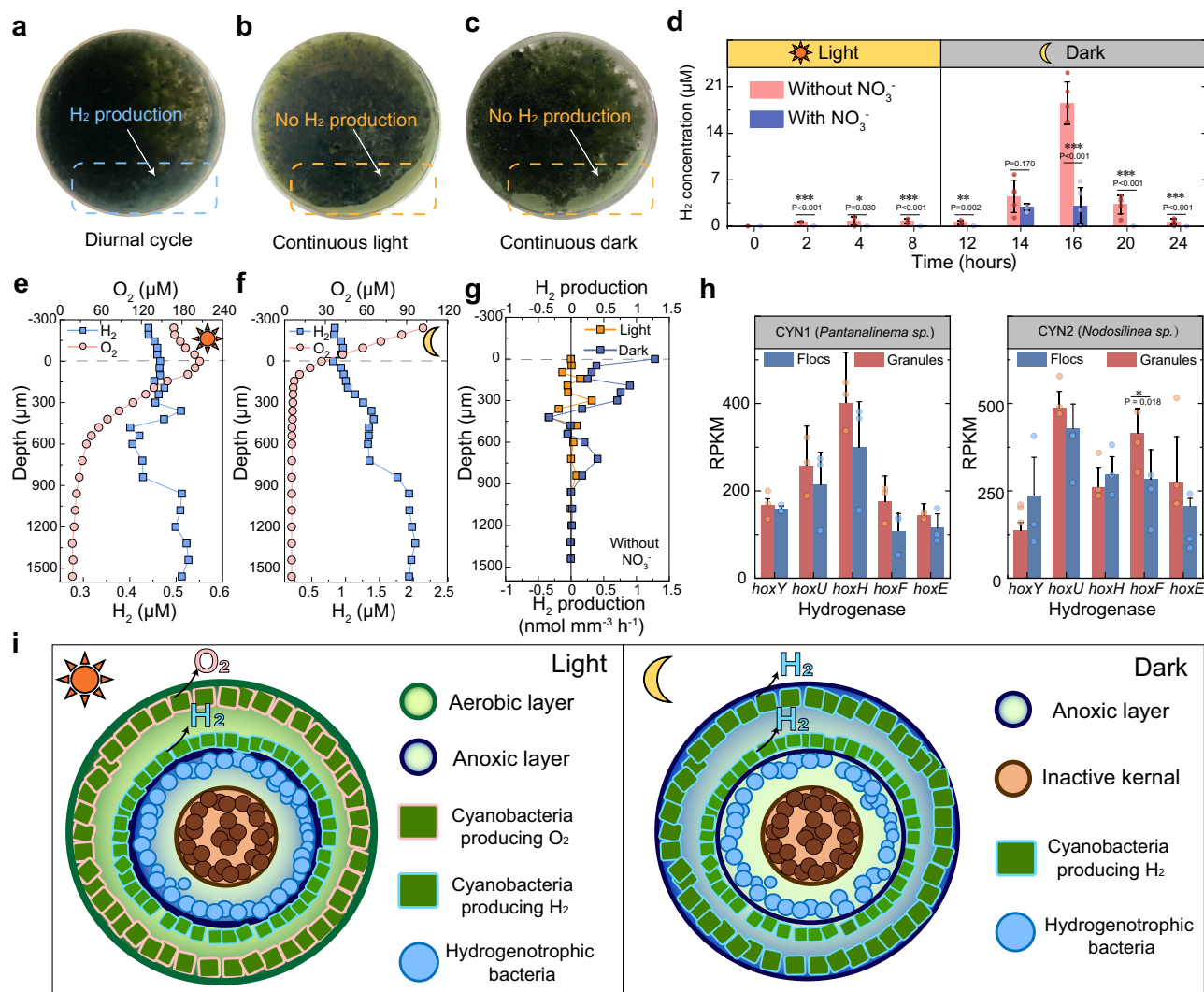


Fig. 3 | Evidence and mechanism for H₂ production in the photogranules.

Photogranule culture media with WO₃ powders under (a) continuous light conditions, (b) continuous dark conditions, and (c) 12-h-light/12-h-dark diurnal cycle. **d** H₂ concentration of photogranule cultures in the headspace under a diurnal cycle with NO₃⁻ (blue) or with NH₄⁺ (red) as the nitrogen source. Data are presented as mean ± SD (*n* = 5). Differences are computed using an unpaired two-sided Student's *t*-test. *, *P* < 0.05; **, *P* < 0.01; ***, *P* < 0.001. The average of three microprofiles of H₂ (blue points) and O₂ (red points) in the photogranule without NO₃⁻ addition under (e) light and (f) dark conditions. **g** H₂ production at each depth is calculated from the microprofiles under light (yellow points) or dark conditions (blue points), assuming a spherical photogranule with a diameter of 3.2 mm. Positive values indicate net production, and negative values indicate the zones of net consumption. The overall H₂ production rate per granule can be calculated by summing the

rates at each depth. **h** The gene expression levels of H₂-evolving bidirectional hydrogenases of the two dominant cyanobacteria in the granule sample (2–5 mm) and floc sample (<0.2 mm). Data are presented as mean ± SD (*n* = 3). Differences were computed using an unpaired two-sided Student's *t* test. *, *P* < 0.05. **i** Schematic of the microbial distribution and internal H₂ cycle in the photogranules under light (left) or dark (right) conditions. There is a layered microbial community and stratified redox conditions in photogranules under light conditions, where aerobic bacteria and nitrifiers consume the oxygen produced by the cyanobacteria in the outer layer and produce H₂. Cyanobacteria generate H₂ under anoxic conditions through photosynthate fermentation, which occurs in the inner layer under light and across all layers in the dark. The produced H₂ is actively used by internal hydrogenotrophic bacteria. Source data are provided with this paper.

in H₂ accumulation (Fig. 3d), which suggests that the nitrogen species also impacts the H₂ production by CA (Supplementary Text 4).

Then, we used microsensors to reveal the spatial distribution of H₂ and O₂ under nitrate-depleted conditions in a single photogranule (diameter of ~3.2 mm, *n* = 5) harvested on the last operational day (Fig. 3e–g). Under light conditions, O₂ concentrations decreased with depth and dropped below 50 μM at depths greater than 600 μm from the granule surface. Conversely, the H₂ concentration varied by ~0.4 μM across the granules (Fig. 3e). In the dark, the H₂ concentration increased with depth to a maximum value of 2.0 μM (Fig. 3f). This concentration is close to previously reported H₂ concentrations (up to 2.3 μM) in deep-sea hydrothermal vents with abundant hydrogenotrophic bacteria³⁶, which highlights the H₂ production potential in

photogranules. H₂ production peaked in the outer layer under dark conditions, and the granular kernels were relatively inactive (Fig. 3g). Summing up the production rates at each depth, the overall net H₂ production rate was 5.19 ± 1.36 nmol granule⁻¹ h⁻¹ under dark conditions. Metatranscriptomic analysis also revealed relatively higher expression of fermentative bidirectional hydrogenase (*hox*) in two dominant cyanobacterial species in the granular sample (2–5 mm) than in the floc sample (<0.2 mm, Fig. 3h). Together, these findings point to an internal H₂ cycle in the photogranules, where cyanobacteria in the photogranules generate H₂ mainly under dark conditions through photosynthate fermentation (Fig. 3i). This process critically depends on the diurnal light exposure (Fig. 3a–c), nitrogen species (Fig. 3d), and size of the aggregates (Figs. 2b and 3h).

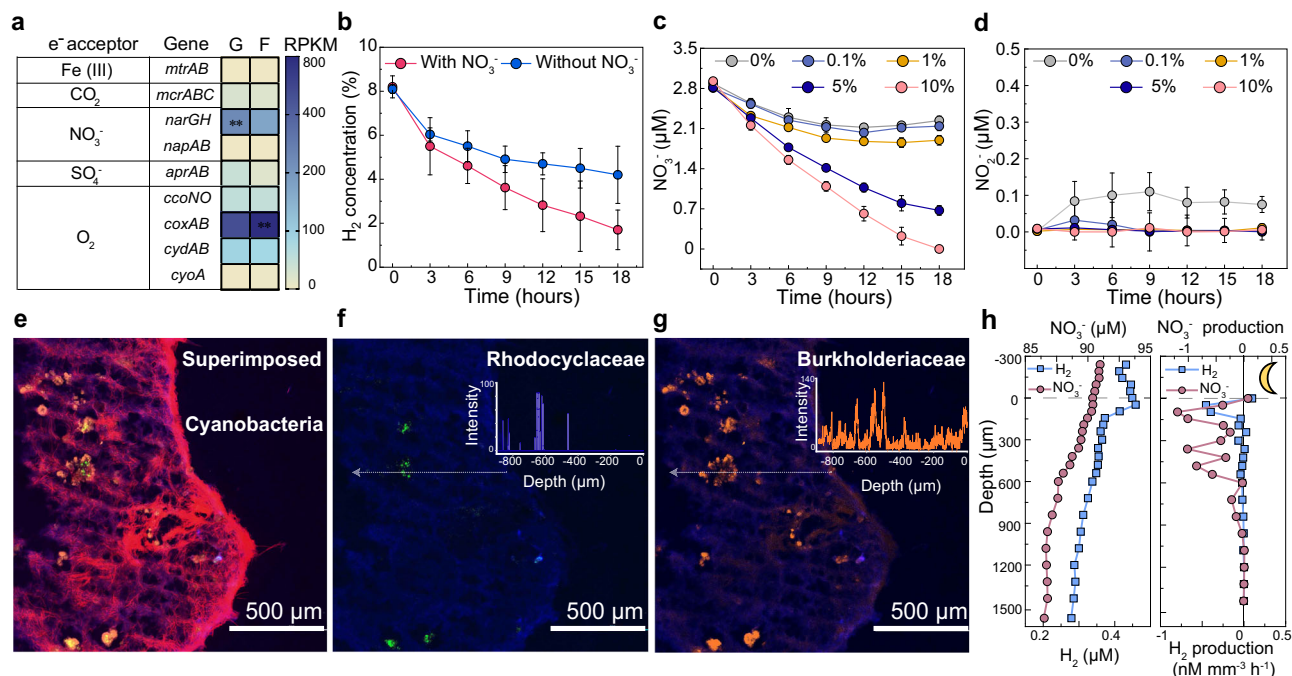


Fig. 4 | Evidence for H_2 consumption by hydrogenotrophic denitrifiers in photogranules. **a** Gene expression of different electron acceptors in the granular sample (G, 2–5 mm, $n = 3$) and floc sample (F, <0.2 mm, $n = 3$) harvested on the last operational day. Heatmaps show the total normalized gene expression (in RPKM). The average RPKM of the two samples is individually shown in two columns. ** represent these two genes over 10× more highly expressed than the other electron acceptor genes. Nitrate (**b**) and nitrite (**c**) consumption profiles of photogranules under different concentrations of H_2 . **d** H_2 consumption profile of photogranules under nitrate replicate and deplete conditions. **e** CLSM image of photogranule

cross-sections showing the spatial distribution of the two main families of hydrogenotrophic denitrifiers: **f** Burkholderiaceae and **g** Rhodocyclaceae. Cyanobacteria shown by self-fluorescence of chlorophyll-a. Lines show the spatial distance of the target microbe to the surface of the CA. **h** The average three microprofiles of H_2 (blue points) and NO_3^- (red points) in the same photogranule under dark conditions (left) when external NO_3^- and H_2 are supplied. Consumption rates (right) of H_2 and NO_3^- at each depth calculated from the microprofiles, assuming a spherical photogranule with a diameter of 3.2 mm. Source data are provided with this paper.

Internal nitrate reducers rapidly consume H_2 in CA

To prove that the hydrogenotrophic denitrifiers were the major consumers of H_2 , we first compared the gene expression levels of possible electron acceptors for H_2 oxidation³⁷. The results revealed that the aerobic oxidase *coxAB* and respiratory nitrate reductase *narGH* were 10× more highly expressed than the other electron acceptor genes, such as sulfate and CO_2 (methanogenesis) (Fig. 4a). Therefore, since O_2 becomes limited in the inner layer of photogranules (Fig. 3f), facultative hydrogenotrophic bacteria may preferentially use nitrate as an alternative electron acceptor for H_2 oxidation. Consistent with the gene expression profiles, depriving photogranules of nitrate considerably reduced the H_2 consumption rate under anoxic conditions (Fig. 4b). A more than 4-fold higher H_2 consumption rate was observed under nitrate-rich conditions than in those without nitrate supply (Fig. 4b). In addition, the nitrate consumption rate increased when the concentration of externally supplied H_2 increased from 0.1% to 10% with almost no accumulation of intermediate NO_2^- (Fig. 4c, d).

Subsequently, fluorescence in situ hybridization (FISH) was applied to characterize the spatial distribution of the dominant hydrogenotrophic denitrifiers in the photogranules harvested on the last operational day (Fig. 4e–g). Burkholderiaceae and Rhodocyclaceae were selected as representative hydrogenotrophic denitrifiers, because they were the two most abundant families of hydrogenotrophic denitrifiers and collectively contributed to over 60% of the H_2 -uptake hydrogenase gene expression (Supplementary Text 5 and Supplementary Fig. 8). The two families existed in tightly packed, mono-species clusters and were predominantly located in the gas channels between cyanobacterial clusters (Fig. 4e). The Burkholderiaceae signal almost entirely overlapped with the Rhodocyclaceae signal, and they coexisted toward the inner layer of the photogranules (Fig. 4e–g),

which suggests that hydrogenotrophic denitrifiers occupy a similar and specific niche in the photogranule. The fluorescent signals of the two families were primarily elevated from the 500 μm (Burkholderiaceae) and 600 μm (Rhodocyclaceae) depths, respectively (Fig. 4f, g). This spatial distribution is consistent with the simultaneous decreases in H_2 and nitrate concentrations that were observed at depths of ~600 μm (Fig. 4h), where O_2 is unavailable (Fig. 3f). This finding indicates that nitrate acts as the main electron acceptor supporting high rates of hydrogenotrophic respiration in the anoxic zone of CA. Considering the net H_2 production rate without nitrate, net H_2 consumption with nitrate and hydrogenotrophic denitrification stoichiometry³⁸, an NRR caused by hydrogenotrophic denitrification up to $3.47 \pm 0.42 \text{ mmol l}^{-1} \text{ day}^{-1}$ was calculated for each granule in the dark (Supplementary Text 6), similar to the overall NRR of the reactor (Fig. 1c). Our results demonstrated that hydrogenotrophic denitrifiers were active in consuming cyanobacteria-derived H_2 to remove nitrate in the inner part of CA (summarized in Fig. 5).

Globally distributed IHT-driven denitrification in CA

To verify the universality of the IHT-driven denitrification in natural environments, we examined whether H_2 -evolving cyanobacteria and hydrogenotrophic denitrifiers co-occurred on the global scale. In addition to photogranules from engineered systems ($n = 13$), CA included bloom colonies from eutrophic lakes ($n = 13$), marine *Trichodesmium* aggregates ($n = 9$), phototrophic mats from hot springs ($n = 12$), and glacier cryoconites ($n = 16$) (Supplementary Data 2). All of these samples coincided with high cyanobacterial abundance (over 5%), where free-living microbes were removed. In addition, we analyzed 60 *Tara* Oceans free-living metagenomes that corresponded to a size fraction of 0.2–3 μm from seawater³ to compare their metabolic

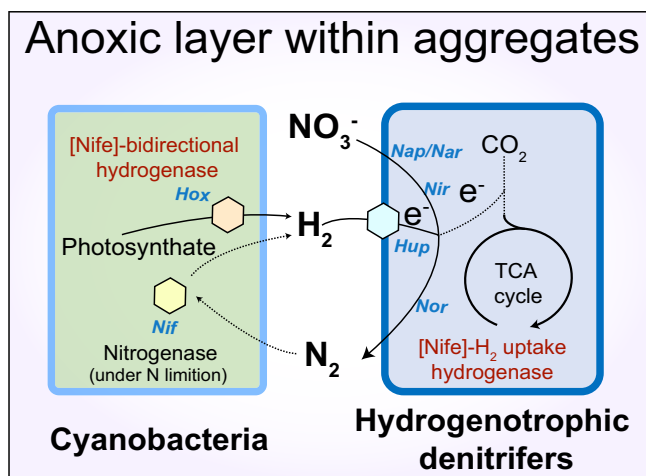


Fig. 5 | Proposed mechanism of IHT-driven denitrification in CA. Cyanobacteria in CA generate H₂ under anoxic conditions through photosynthate fermentation catalyzed by [Nife] bidirectional hydrogenase (*Hox*). Hydrogenotrophic denitrifiers oxidize H₂ coupled with the reduction of nitrate to gain energy. The dashed line represents the possible reaction when nitrogen is absent: Some cyanobacteria can generate H₂ through nitrogen fixation, and the produced H₂ may be used by hydrogenotrophic bacteria to support carbon fixation and growth.

potential (Supplementary Fig. 9). Overall, the potential for IHT-driven denitrification was widespread among the analyzed CA. MAGs of both H₂-evolving cyanobacteria and hydrogenotrophic denitrifiers were detected in 84% of the 63 CA samples (Fig. 6a and Supplementary Data 3). The gene abundance of H₂-uptake hydrogenase was up to 4 orders of magnitude higher in the cyanobacterial aggregates (CA) compared with that of free-living microbes in H₂-supersaturated seawater (Fig. 6b), which suggests a relatively high H₂ concentration at global CA. Fermentative bidirectional hydrogenase was found to constitute the main H₂-evolving pathway of cyanobacteria in most CA, despite N fixation is the primary mechanism for H₂ production in marine *Trichodesmium* aggregates (Supplementary Data 4). Importantly, the linear correlation analysis confirmed that the gene abundance of H₂-uptake hydrogenase significantly increased with the gene abundance of H₂-evolving hydrogenase ($R^2 = 0.80$, $P < 0.001$) in CA (Fig. 6c). In addition, the gene abundances of nitrate reductase and H₂-uptake hydrogenase were significantly correlated ($R^2 = 0.25$, $P < 0.001$; Fig. 6d) in CA. Meanwhile, the ratio of hydrogenotrophic denitrifiers to all denitrifiers (in terms of the MAG amount) was ~25–58% in different CA samples but less than 10% in the free-living microbes (Supplementary Fig. 10). Together, these results suggest that CA provides a unique niche for hydrogenotrophic denitrifiers in the natural environment.

To better understand the basis of these activities in global CA, we used homology-based searches to determine the abundance of key metabolic marker genes in the metagenomic assemblies³. The H₂-uptake hydrogenase was encoded by 48% (engineered system), 17.6% (lake), 28.1% (marine), 34.6% (hot spring), and 5% (glacier) of CA-associated bacteria on average (Fig. 6e). The MAGs that encode H₂-uptake hydrogenases spanned more than 20 bacterial phyla in those CA (Supplementary Data 3). The hydrogenotrophic denitrifiers in those CA were mainly Burkholderiaceae (lakes, hot springs, and engineered systems), Rhodobacteraceae (marine), Rhodocyclaceae (hot springs and engineered systems), and Saprospiraceae (glacier, hot springs, and engineered systems; Supplementary Data 3). In addition, we performed molecular clock dating to explore the penitential origin of the representative hydrogenotrophic denitrifiers (Rhodobacteraceae and Burkholderiaceae) from global CA. The divergence time of two main hydrogenotrophic denitrifiers, Rhodobacteraceae (1.74 Ga)

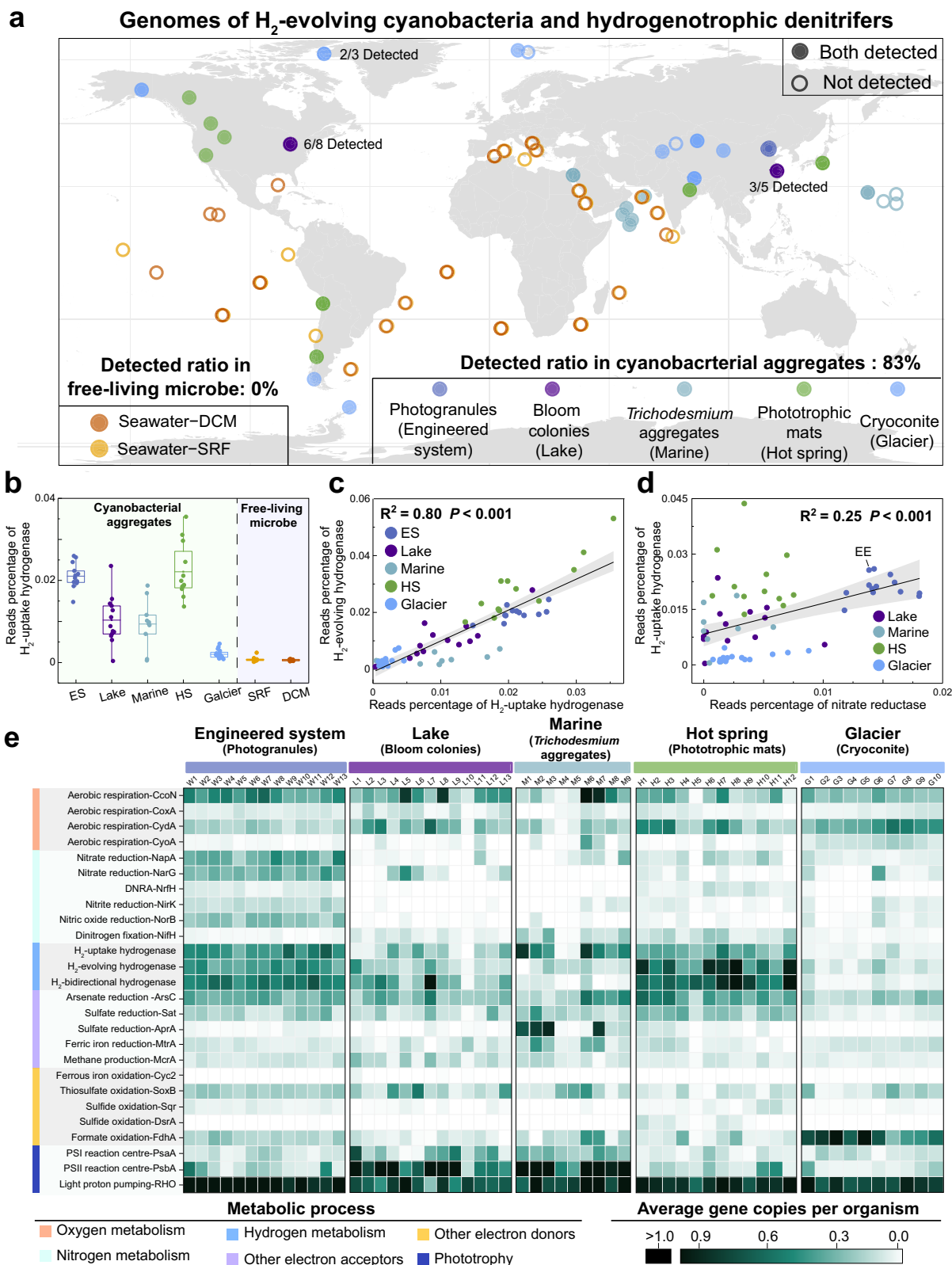
and Burkholderiaceae (1.66 Ga), diverged around 1.7 Ga (Supplementary Fig. 11), which suggests that hydrogenotrophic denitrification is an energy acquisition trait on the early Earth.

The abundance of nitrate reductase varied among different samples and likely depended on the local nitrate concentration. In addition, we observed an enrichment of sulfate reduction (*sat*, *aprA*) and methanogenesis genes (*mcrA*) in the samples without the detection of nitrate reductase (Fig. 6e), especially in bloom colonies and marine *Trichodesmium* aggregates. Sulfate reduction or methanogenesis may become the major sink of H₂ when nitrate is depleted in the environment³⁹. In comparison to other habitats that have been tested, most CA from eutrophic lakes (L4, L5, L6, L11, and L13) and hot springs (H1, H4, H6, H7, H8, and H10) were identified as potential hotspots for hydrogenotrophic denitrification, since both nitrate reductase and H₂-uptake hydrogenase were encoded by more than 15% of bacteria in these environments (Fig. 6e). Collectively, our analyses suggest that IHT appears to drive nitrate reduction and nitrogen loss in globally distributed CA.

Discussion

Hydrogenotrophic denitrification has emerged as a clean autotrophic technology for engineered nitrogen removal⁴⁰. However, the low H₂ concentration and solubility in natural aquatic ecosystems have caused the underestimation of its contribution to nitrogen loss. Although the role of cyanobacteria-produced H₂ as a renewable energy source has been well studied⁴¹, its impact on neighboring bacteria and the nitrogen cycle has been largely overlooked. Here, we propose that cyanobacteria-derived H₂ is a critical electron source for symbiotic bacteria that reside in globally distributed CA, potentially drives the nitrate reduction, and unveils a previously unrecognized pathway for nitrogen loss in aquatic ecosystems. Our study demonstrated the enrichment of hydrogenotrophic denitrifiers using in situ H₂ produced in engineered photogranules. Autotrophic photogranules offer a sustainable alternative to remove residual nitrate in the effluent of wastewater treatment plants without the external electron donors.

Nitrogen loss in aquatic ecosystems has long focused on heterotrophic denitrification and should be re-examined with a focus on hydrogenotrophic denitrification. In the contemporary ocean, there is a nitrate deficit of ~2 mmol l⁻¹ if the Redfield ratio is assumed⁴². The IHT-driven denitrification may explain the increasing nitrogen loss and nitrate deficit, which are accompanied by intensified eutrophication that leads to the expansion and persistence of CA. Studies have demonstrated that lake hotspots of N loss are commonly eutrophic lakes⁴³, where cyanobacterial blooms promote the N export, and carbon-coupled heterotrophic denitrification is considered the primary mechanism⁴⁴. Compared with organic carbon, H₂ is a more easily diffusing electron donor that requires minimal cellular resources for use and provides more energy per electron during nitrate reduction⁴⁵. In this study, hydrogenotrophic denitrification caused an N loss rate of 3.47 ± 0.42 mmol l⁻¹ day⁻¹ (-1.85 mmol m⁻² day⁻¹) in the engineered CA. The IHT-driven denitrification rate was greater than 50% of the heterotrophic denitrification rate of the traditionally engineered system²⁴ and relatively higher than the N loss rate of heterotrophic denitrification in marine sediment (0.5 – 2.0 mmol m⁻² day⁻¹)⁴⁶. In addition to engineered CA (0.4 – 2.0 μM H₂), coastal cyanobacterial mats (30 – 40 μM H₂)¹⁴ and marine *Trichodesmium* colonies (0.2 – 0.6 μM H₂)¹³ also have high internal H₂ concentrations, which are potentially sufficient to support nitrate reduction comparable to those in our study. Although heterotrophic denitrification is predominant in many aquatic ecosystems, we suggest that hydrogenotrophic denitrification can be an essential route for nitrogen loss where cyanobacterial blooms and aggregates are common. Considering the global prevalence of CA, the IHT-driven denitrification can substantially contribute to nitrogen loss in eutrophic waters. Given that this study only uses global metagenomic analysis for the generalities of IHT-driven denitrification,



activity-based measurements of global CA are needed to robustly verify its wider significance.

The cyanobacterial-bacterial IHT may also act as a vital mechanism for the evolution of hydrogenotrophic microbes and denitrification pathways on the early Earth. Hydrogenotrophic microorganisms are considered among the earliest cellular life forms that colonized our planet^{2,47}. However, the availability of H₂ became limited with Earth's

oxidation, and some hydrogenotrophic microbes relied on H₂-evolving organisms for survival⁹. Thus, the evolution of cyanobacteria with their ability to produce H₂ possibly supported ancient hydrogenotrophic microorganisms¹⁶. Due to the low primary productivity during the Boring Billion (0.8–1.8 Ga)⁴⁸, the organics are limited, and heterotrophic denitrification played a relatively minor role in nitrogen loss on the early Earth⁴⁹. Marine heterotrophic bacteria emerge until

Fig. 6 | Metabolic potential for IHT-driven denitrification at the global scale CA. **a** World map of the sample distributions of different types of CA or free-living *TARA* ocean samples in this study. The point color shows whether the genomes of H_2 -evolving Cyanobacteria (encoding hydrogenase or nitrogenase) and hydrogenotrophic denitrifier consumers (encoding both H_2 -uptake hydrogenase and *narG/napA*) were isolated at that location. The number of presented samples is noted if a site has multiple samples without all being present. **b** Gene abundance of H_2 -uptake hydrogenases in different samples. ES, engineered system ($n = 13$); lakes ($n = 13$); marine ($n = 9$); HS, hot spring ($n = 12$); glacier ($n = 16$); SRF, surface ($n = 12$); DCM, deep chlorophyll maximum ($n = 12$). Boxplot: center line, median; box limits, upper and lower quartiles; whiskers, $1.5 \times$ interquartile range. Gene abundance was present in percentage of sequence reads identified within 1 million random metagenome reads. **c** Linear correlation between gene abundance of H_2 -evolving

hydrogenase and H_2 -uptake hydrogenase in global CA. Black lines indicate the fitted linear models with confidence intervals of 0.95 (grey area). Pearson correlation coefficients are shown, two-sided tests are used for alternative hypothesis testing ($n = 63$ biologically independent samples). **d** Linear correlation between gene abundance of H_2 -uptake hydrogenase and nitrate reductase (sum of *narG* and *napA*) in the global CA sample. Black lines indicate the fitted linear models with confidence intervals of 0.95 (grey area). Pearson correlation coefficients are shown, two-sided tests are used for alternative hypothesis testing ($n = 63$ biologically independent samples). **e** Abundance of metabolic marker genes based on the metagenomic short reads across the global cyanobacterial aggregates. Homology-based searches are used to calculate the relative abundance of marker genes as average gene copies per organism for the metagenomes (abundance relative to a set of universal single-copy genes). Source data are provided with this paper.

-0.4 – 0.8 Ga⁴⁹, which is much later than hydrogenotrophic bacteria in this study (~ 1.7 Ga). This suggests that hydrogenotrophic denitrification may have driven the evolution of bioenergetic pathways related to modern denitrification. The microenvironments of CA and their diverse function (i.e., H_2 -evolution, N fixation, nitrification) provide a unique niche for the potential evolution of hydrogenotrophic denitrifiers⁵⁰. CA acts as living fossil to preserve diverse ancient microbes and metabolic functions via H_2 -based syntrophic sinks. The IHT between cyanobacteria and symbiotic bacteria may account for that some ancient H_2 -consumers, such as *Chloroflexota*⁵¹, are now still found to form close physical associations with cyanobacteria CA⁵². We suggest that the IHT-driven denitrification in CA may have had a potentially profound influence on the nitrogen cycle for more than half of Earth's history. Finally, cultivation and enrichment of H_2 -evolving cyanobacteria and hydrogenotrophic denitrifiers from different types of CA will shed further light on the IHT-driven nitrogen cycle.

Methods

Engineered nitrogen removal system set-up and sampling

A photo-sequencing batch bioreactor with a working volume of 4 l was started by inoculating 3 g l^{-1} (in terms of mixed liquor suspended solid concentration) of the activated sludge collected from the aeration tank of a local municipal wastewater treatment plant. An LED light board ($\lambda = 400$ – 840 nm) is positioned above the reactor, providing a light intensity of $200 \pm 50 \mu\text{mol m}^{-2} \text{ s}^{-1}$ at the reactor's surface. The reactor was fed with synthetic wastewater with $100 \pm 5 \text{ mg l}^{-1} \text{ NH}_4^+\text{-N}$ and the following nutrients per liter: 500 mg NaHCO_3 , 100 mg CaCl_2 , 60 mg MgSO_4 , $60 \text{ mg KH}_2\text{PO}_4$, 10 mg FeSO_4 , and 1 ml trace solution (Na_2EDTA , 15 g ; $\text{ZnSO}_4 \cdot 7\text{H}_2\text{O}$, 0.43 g ; $\text{CoSO}_4 \cdot 7\text{H}_2\text{O}$, 0.283 g ; $\text{MnSO}_4 \cdot \text{H}_2\text{O}$, 0.845 g ; $\text{CuSO}_4 \cdot 5\text{H}_2\text{O}$, 0.25 g ; $\text{NiCl}_2 \cdot 6\text{H}_2\text{O}$, 0.19 g ; H_3BO_3 , 0.014 g per liter). No external aeration was applied, and the homogenization was maintained by magnetic stirring at 200 rpm . The reactor was operated in three stages at room temperature for 400 days. In Phase 1 (Days 0–70, start-up phase), $100 \pm 5 \text{ mg l}^{-1} \text{ COD}$ in the form of sodium acetate was added to the influent medium as the electron donor to make a C: N of 1: 1, the reactor was operated in a cycle of 12–24 h including feeding (10 min), mixing (11.5–23.5 h), settling (10 min), and discharging (10 min). The hydraulic retention time (HRT) was gradually adjusted according to the reactor performance. In Phase 2 (Days 71–220, heterotrophic phase), each cycle was set to 24 h. The HRT and the light/dark period were fixed to 36 h and 12 h light/12 h dark diurnal cycle, respectively. In Phase 3 (Days 221–400, autotrophic phase), COD was deprived from the influent to transition to an autotrophic nitrogen removal system. A mesh separator with a $200 \mu\text{m}$ screen was used to retain the granules in the effluent.

Influent and effluent samples were collected through the $0.22 \mu\text{m}$ filters every 4 days for analyzing ammonium ($\text{NH}_4^+\text{-N}$), nitrite ($\text{NO}_2^-\text{-N}$), nitrate ($\text{NO}_3^-\text{-N}$) using a flow injection analyser (Quik Chem, Lachat Instruments, USA). VSS and mixed liquor suspended solids (MLSS) concentration were measured using an automatic moisture and ash analyser (prepASH 340, Precisa, Switzerland). The MLSS refers to the

biomass concentration in the sequencing batch reactor⁵³ and can represent the biomass of CA. The granular size was analyzed through imaging by microscope (Olympus, CKX53, Japan) using the software ImageJ^{54,55}. During reactor operation, biomass was collected through centrifugation for metagenomic sequencing to track time-series changes of hydrogenases and hydrogenotrophic bacteria. On specific days (0, 20, 40, 60, 80, 150, 220, 300, and 400), 50 ml mixed biomass was collected through centrifugation ($7000 \times g$ for 5 min) for metagenomic analysis. Metatranscriptomic samples for flocs and granules (3 replicates for each sample) on the last operational day (day 400) were harvested to explore the transcriptional activity of hydrogenases in the stable phase. Flocs sample ($<0.2 \text{ mm}$), and granular sample (2 – 5 mm) were segregated through mesh⁵⁶, this threshold allows us to better understand the differences in transcriptional activity between aggregates and planktonic organisms under similar environmental conditions. The sampled biomass was instantly frozen in liquid nitrogen and stored at -80°C for further DNA or RNA extraction. At the end of the reactor operation (on Day 400 ± 5) when biomass concentration was stable (Supplementary Fig. 12), mixed biomass was collected through centrifugation ($5000 \times g$ for 5 min) for nitrogen balance calculation and batch tests. Photogranules ranging from 2 to 5 mm were collected through a mesh separator for FISH and environmental scanning electron microscopy (Quanta, Thermo Scientific, USA), microsensor measurement.

Nitrogen balance calculation

The total inorganic nitrogen loading rate (NLR), NRR, and nitrogen removal efficiency were calculated according to the following equation.

$$\text{NLR} = \text{TIN}_{\text{eff}} / \text{HRT} \quad (1)$$

$$\text{NRR} = (\text{TIN}_{\text{eff}} - \text{TIN}_{\text{inf}}) / \text{HRT} \quad (2)$$

$$\text{Nitrogen removal efficiency} = (\text{TIN}_{\text{eff}} - \text{TIN}_{\text{inf}}) / \text{TIN}_{\text{eff}} \quad (3)$$

Where TIN_{inf} and TIN_{eff} (in $\text{mM l}^{-1} \text{ day}^{-1}$) refer to the sum of $\text{NH}_4^+\text{-N}$, $\text{NO}_2^-\text{-N}$, and $\text{NO}_3^-\text{-N}$ concentrations of influent and effluent, respectively.

To elucidate the contribution of nitrification-denitrification and assimilation to nitrogen removal, batch tests were conducted by adding the nitrifying inhibitor ATU. The addition of ATU inhibits nitrification pathway without impacting assimilation⁵⁷, thus the nitrogen removal with ATU addition can be attributed to microbial assimilation (Supplementary Text 1)⁵⁸. In the experimental group, 10 mg l^{-1} ATU was added to negate the nitrification-denitrification process in nitrogen removal. The control group did not receive ATU. For each condition, triplicate mixed biomass of 150 ml ($\sim 0.29 \text{ gVSS}$) was collected from the reactor, washed with PBS solution, and then placed into 200 ml glass cylinders containing 150 ml synergetic medium

(same with the reactor influent). These cylinders were incubated on a rolling table at 150 rpm for 24 h under conditions mirroring those of the reactor. The nitrogen removal of nitrification-denitrification can be derived from the difference between the control group and the experiment group.

To explore the contribution of fermentative organic products from photogranules to denitrification, a second set of batch tests was conducted by adding soluble fermentative products collected (Supplementary Text 7)⁵⁹. In brief, 100 ml biomass (~0.19 gVSS) was collected and rinsed at the end of the reactor's light phase and transferred to a 400 ml sealed serum vial. The vials were securely sealed with butyl rubber stoppers and aluminum caps, then purged with argon. 100 ml pre-collected soluble fermentative products were used as the culture medium for the experimental group. Same volume of sterilized water was used as the culture medium in the control group. Each group was inoculated under dark anoxic conditions for 15 h in triplicate. All the culture medium was supplemented with 3.6 mM NO₃⁻ (in the form of sodium nitrate), and the nitrate concentration was monitored by periodically sampling 1 ml of the liquid.

Metagenome sequencing and analysis

DNA extraction was conducted utilizing the FastDNA Spin Kit for Soil (MP Biotechnology, CA, USA). The purity and yield of the DNA were verified via Nanodrop 1000 spectrophotometer (IMPLEN, CA, USA). Subsequent paired-end sequencing was carried out on an Illumina HiSeq 4000 platform (Illumina Inc., San Diego, CA, USA) at Majorbio Bio-Pharm Technology Co., Ltd. (Shanghai, China), employing both the HiSeq 4000 SBS Kits and 4000 PE Cluster Kit, following the manufacturer's guidelines (www.illumina.com). The raw metagenomic reads were firstly trimmed by removing the adaptor sequences and ambiguous nucleotides using SeqPrep v1.1⁶⁰ based on default parameters, and the trimmed sequences were quality filtered using Sickle v1.33 based on a minimum quality score of 20 and a minimum sequence length of 50 bp⁶¹. Contigs and scaffolds were then assembled individually for each sample using IDBA-UD with default parameters⁶². Coverage profiles for each contig were generated using BBMap v37.75 by mapping the short reads to the assemblies⁶³.

The scaffolds generated were binned into the metagenome-assembled genomes (MAGs) based on abundance and the tetranucleotide frequency using MetaBAT2 with the sensitive model. The relative abundance of each MAG was calculated using BBMap v37.75 by mapping the MAGs to the raw metagenome reads⁶³. For short-read-based metagenomic analysis of the microbial community in the reactor, the read-based relative abundance of the taxonomic unit was calculated using metagenome reads by Kaiju v1.7.2 and BLAST against the NCBI-nr database (2021-03-29)⁶⁴. Phylosift v1.0.1 was used to construct the phylogenetic tree of MAGs based on the 37 marker gene families in each genome using the default parameters⁶⁵. The 37-protein sequence from the genomes was aligned using MAFFT v7.222 with default parameters⁶⁶. Molecular Evolutionary iTOL v6.0 website (<https://itol.embl.de/>) was used to visualize the phylogenetic tree. MAGs were dereplicated with dRep v3.2.2 with the default 99% average nucleotide identity flag to produce a final collection of non-redundant genomes⁶⁷. The rarefaction analysis of non-redundant medium-quality MAGs (>70% completeness and ≤10% contamination) as a function of the input samples was performed to demonstrate coverage⁶⁸. MAGs with completeness >90% and contamination <10% were used for downstream analysis. As no eukaryotic MAGs were recovered in this study, taxonomic annotation of prokaryotic MAGs was performed using GTDB-Tk v1.7.0 with GTDB release 214⁶⁹.

Metabolic annotation

Functional annotations of MAGs were conducted together using the Metabolic v4.0⁷⁰, and compared against the eggNOG database with an e-value cutoff of 1e⁻⁵ using eggNOG-mapper v5.0⁷¹. Based on the

annotation tools, the proteins of specific interest were manually refined. The sequences of hydrogenases were further classified using HydDB²⁵. Matched reads for hydrogenase are recorded as relative percentage abundance within 1 million random metagenome reads²⁵.

Metatranscriptomic analysis

Total RNA was extracted from triplicate using the E.Z.N.A.[®] Soil RNA Midi Kit (Omega BioTek, Norcross, GA, US) in strict adherence to the manufacturer's guidelines. The purity and yield of the RNA were verified via a Nanodrop 1000 and a Qubit Fluorometer. Total RNA then underwent rRNA removal using the Ribo-Zero Magnetic Kit, following the manufacturer's instructions (Epicentre, an Illumina[®] company). Subsequently, cDNA libraries were prepared using the TruSeq[™] RNA Sample Prep Kit (Illumina). These barcoded libraries were then sequenced in a paired-end format on the Illumina HiSeq 3000 platform at Majorbio Bio-Pharm Technology Co., Ltd (Shanghai, China), employing the HiSeq 4000 PE Cluster Kit and HiSeq 4000 SBS Kits as per the manufacturer's guidelines (www.illumina.com). Non-rRNA reads were mapped to all MAGs using BBMap v37.75⁶³. For gene expression within the MAGs, read counts of each gene were calculated using HTSeq-count v0.9.1⁷². The read counts were then corrected for gene length and the total number of reads in the transcriptome dataset to obtain the RPKM⁷³. Short-read-based metagenomic and metatranscriptomic analysis for gene abundance was calculated from raw metagenomic and metatranscriptomic reads recruitment numbers by normalizing reads and length to obtain the RPKM⁷³.

Phylogenetic analysis of hydrogenase

The phylogenetic tree was constructed to understand the diversity of hydrogenase recovered from the high-quality MAGs of CA. The amino acid sequences encoding the large subunits of [NiFe] hydrogenases and present in the genomes of our dataset were aligned with MAFFT v7.222⁶⁶. Finally, a maximum likelihood phylogenetic tree was conducted using IQ-TREE v2.0 with the best-fit LG + C20 + R + F as the best-fit model selected by ModelFinder⁷⁴ and 1000 ultrafast bootstrap⁷⁵. The transcriptional abundance of each hydrogenase sequence in the metatranscriptomic sample of granules was represented with log₁₀(RPKM + 1). Phylogenetic tree visualization was performed using the iTOL v6.0 website (<https://itol.embl.de/>).

Analysis of H₂ production

The presence of H₂ was first detected by the WO₃³³. Fifty microliters biomass (~0.095 gVSS) from the reactor was directly transferred to 100 ml serum bottles, which were cultured under a light intensity of 200 μmol m⁻² s⁻¹ in three conditions: continuous light, continuous dark, and 12 h light/12 h dark diurnal cycle. 0.1 g WO₃ powders (size ≤ 100 nm, Sigma-Aldrich) were added to the serum bottles to examine the presence of H₂ in the medium. The cultures were incubated for 48 h, and the medium was exposed to air. WO₃ reacts with H₂ to produce tungsten bronze as an indicator for H₂ presence, undergoing a color shift from light yellow to blue-gray upon reacting with H₂³³.

H₂ production in diurnal cycles under both 3.6 mM NO₃⁻ (in the form of sodium nitrate) and 3.6 mM NH₄⁺ (in the form of ammonium chloride) conditions was monitored by the gas chromatography method. For each condition, 3 replicate vials were prepared identically for each group. One hundred milliliters biomass (~0.19 gVSS) was collected at the end of the reactor's light phase and transferred to a 400 ml sealed serum vial capped with butyl rubber stoppers. Each vial contained 100 ml of culture medium. Three hundred milliliters headspace of the serum vials was left as ambient air for light/oxic incubations and was purged with argon for dark/anoxic incubations. At each time point, 3 ml gas was extracted from at least five replicate vials and stored in pre-evacuated 3 ml silicone-sealed Exetainers. H₂ from headspace gas was quantified by gas chromatography (Agilent 7890, USA) equipped with a molecular sieve 5A column and a helium

ionization detector (D-4-I-SH14-R, Valco Instruments, USA) with helium carrier and makeup gas. The volume fractions (in ppm) of H_2 determined by gas chromatography were used to calculate the amount of H_2 by applying the ideal gas law⁷⁶. To prove the major role of cyanobacteria in H_2 production within photogranules, the most dominant cyanobacteria were isolated, and H_2 production by cyanobacteria isolates was also tested (Supplementary Text 3).

Microsensor measurement

Internal H_2 , O_2 , and NO_3^- concentration of the photogranules under light ($200 \mu\text{mol m}^{-2} \text{s}^{-1}$) or dark conditions was determined using microsensors (Unisense, Denmark) fitted to a motorized micromanipulator. Photogranules with an average diameter of 3.2 mm were harvested using the sieve at the end of the light phase from the reactor. After previous illumination ($200 \mu\text{mol m}^{-2} \text{s}^{-1}$) treatment for 1 h, photogranules were pinned with glass needles to a nylon mesh fitted over a small petri dish. The photogranules were then rapidly immersed in the previously stored N_2 -flushed reactor influent ($DO = 0-0.5 \text{ mg l}^{-1}$, $NH_4^+ = 3.6 \pm 0.1 \text{ mM}$, no acetate) and amended with 1 wt% agar. To test the H_2 and NO_3^- consumption profile under dark conditions, $200 \pm 20 \mu\text{M } NO_3^-$ was added to the substrate, and 10 ml 100% H_2 was injected into the medium. The microsensor was previously calibrated, and the step size of the micromanipulator was 48–120 μm when the tips of the microsensors were piercing the central photogranules (Supplementary Fig. 13).

Using the H_2 profiles generated from the microsensor measurements, the net consumption/production rates of reactants within photogranules were calculated by segregating the photogranule into shells²³. The size of the shell corresponded to the width of the interval between measurements, with the assumption of a spherical geometry for the granule. The flux between a point on the exterior of the shell and a point on its interior was computed and subsequently multiplied by the shell's surface area to ascertain the net rate of reaction according to the following equation:

$$P = D \times (dCr/dXr) \times 4 \times \pi \times r^2 \quad (4)$$

where P represents the interfacial flux (expressed in nmol/h), D is the diffusion coefficient ($4.3 \times 10^{-9} \text{ m}^2 \text{s}^{-1}$ for H_2 at 25°C ⁷⁷), dCr/dXr represents the concentration gradient of the reactant at location r , and r the radial distance from the shell surface to the center of the aggregate. The total conversion rates were obtained by the addition of activities in all shells, the production rate of each shell was divided by its corresponding volume to calculate the volumetric rate^{13,23}.

Ex situ H_2 -utilization activity assays

To determine the activity of hydrogenotrophic denitrifiers in the photogranules, H_2 consumption rates of photogranules were compared under nitrate-replete (with $\sim 3.6 \text{ mM } NO_3^-$ in the form of sodium nitrate) and nitrate-deplete condition in triplicate. For each group, 100 ml biomass ($\sim 0.19 \text{ gVSS}$) was centrifuged at the end of the reactor's light phase and transferred to a 400 ml sealed vial containing 100 ml of substrate (same as the reactor influent, despite the N source). The vials were securely sealed with butyl rubber stoppers and aluminum caps, then purged with argon to create anoxic conditions for the incubation. Vials were incubated at room temperature on an orbital shaker at 150 rpm to ensure that photogranules were constantly in motion and well-mixed. H_2 consumption was monitored by periodically sampling 3 ml gas from the headspace, and their content was measured by gas chromatography as described above.

To evaluate the maximum activity of hydrogenotrophic denitrifiers within photogranules, external H_2 was supplied with initial gaseous volume percentages of 0%, 0.1%, 1%, 5%, and 10% (mixed with argon) to test the nitrate reduction rate. Substrate amended with

$3.6 \text{ mM } NO_3^-$, 0.5 g l^{-1} of $KH_2PO_4 \cdot 2H_2O$, and 2.5 g l^{-1} of $K_2HPO_4 \cdot 7H_2O$ (as buffers) was used as culture medium. Other experiment setups and conditions are same as the activity test. NO_3^- and NO_2^- consumption was monitored by periodically sampling 1 ml of the liquid. Samples were withdrawn from the vials after careful flushing of needles and syringes with Ar to avoid oxygen contamination.

FISH staining and confocal laser scanning microscopy (CLSM)

The spatial localization of pivotal hydrogenotrophic denitrifiers in the photogranules was analyzed by FISH. Photogranules underwent washing and subsequent fixation in 4% paraformaldehyde for 4 h at 4°C . Following dehydration, the samples were encased in an optimum cutting temperature compound overnight, then sectioned into 60 μm slices using a cryostat at -20°C (Leica CM1950, Germany). The probes for hybridization included Cy3 (orange) -labeled Burkho for Burkholderiaceae family⁷⁸, and Alexa Fluor 488 (green)-labeled RHC439 for Rhodocyclaceae family⁷⁹. The distribution of cyanobacteria and microalgae was observed by the spontaneous fluorescence of chlorophyll-a (red). Visualization of FISH-processed samples was achieved with a Zeiss LSM980 confocal laser scanning microscope (Carl Zeiss, Germany). Finally, the spatial distance of the target microbe was calculated using ImageJ software⁸⁰.

Global metagenomic data collection and analysis

We collected 63 CA metagenomic samples in July 2023 from the Sequence Read Archive (SRA) database, including photogranules from the engineered system, lake bloom colonies, phototrophic mats from hot springs, glacier cryoconites, and marine *Trichodesmium* aggregates (Supplementary Data 2). Those samples correspond with high cyanobacteria abundance (the relative abundance of cyanobacteria was over 5% in the identified microbial community in the short read). We carefully checked the sampling method from the reference studies of each raw data to ensure that the free-living microbes were removed. The relevant sampling strategy for each data was summarized in Supplementary Text 8. Only the metagenomes sequenced by the shotgun sequencing using the Illumina platform were chosen to avoid platform bias. To ensure the quality of data, sequences were required to have a higher average spot length value than 150 and a size greater than 500 M. In addition, 60 Tara Oceans free-living metagenomes corresponded to a size fraction of 0.2–3 μm of seawater to compare their metabolic potential (Supplementary Data 5). Detailed information on these metagenomic samples is available in Supplementary Data 2 and 5.

For short-read-based analysis in the global CA dataset, contig-based gene abundance was calculated by dividing gene abundance by the mean abundance of single-copy ribosomal marker³. Short reads from different samples were assembled into contigs individually with IDBA-UD. For comparison of gene abundance from contigs, gene abundance in the short reads of each sample was normalized as average gene copies per organism. The abundance was calculated by dividing gene abundance (in RPKM) by the mean abundance of 14 universal single-copy ribosomal marker genes sourced from the SingleM v0.15.0 (<https://github.com/wwood/singlem>). This reflects the percentage of community members harboring the gene for single-copy metabolic genes³. The total of H_2 -evolving hydrogenase and H_2 -uptake hydrogenase was aggregated from all hydrogenases predicted to possess H_2 -evolving ([NiFe] groups 3, 4; [FeFe] groups A, B) or H_2 -uptake ([NiFe] groups 1, 2a, 3) functions, as classified by HydDB²⁵. Linear correlation analysis was employed to assess the correlation of gene abundance among these groups. Genome binning, refinement, and metabolic annotation were performed according to the same protocol used above; MAGs with completeness > 50% and contamination < 10% were used for downstream analysis. A linear correlation analysis was performed to determine how metagenomic gene abundance correlated.

Molecular clock analysis

To date the divergence times of the representative hydrogenotrophic denitrifiers in CA, we performed molecular clock analysis using the program MCMCTree from the PAML package v4.9j⁸¹. Given that MAGs affiliated with Rhodobacteraceae and Burkholderiaceae were dominant hydrogenotrophic denitrifiers in the global CA metagenomes, we selected all 23 MAGs affiliated with the above two families together with 37 reference bacterial genomes for molecular clock dating. The phylogenetic analysis was based on a concatenation of 26 single-copy genes present in over 90% of MAGs (Supplementary Data 6). Those genes are part of the set of 71 bacterial single-copy genes from GToTree⁸² that show little horizontal transfer and, therefore, are suitable for molecular clock dating analysis⁸³. The sequences of each gene were aligned with MAFFT v7.222⁶⁶, and a maximum-likelihood phylogenetic tree was inferred using IQ-TREE v2.0 with LG + C60 + F + G and 1000 UFBoot branch test replicates. The dating analysis was performed with the Bayesian relaxed clock model implemented in MCMCTree⁸¹, and the iteration parameters burn-in: 10,000; sampling 211 frequency: 50; number of samplings: 50,000. The convergence of the molecular dating analysis was evaluated by comparing the posterior dates of two independent runs⁴⁹. The estimated divergence times across runs showed high consistency, with a maximum relative difference of less than 0.1 Ga between runs for the key nodes of hydrogenotrophic denitrifiers. The used reference genomes and node age for calibration are shown in Supplementary Text 9 and Supplementary Fig. 11.

Statistical analysis

Statistical analyses were performed using R v4.2.3. The psych package was used to make Spearman's correlation matrix among environmental factors and hydrogenase abundance. The world maps were generated using the publicly available simple features⁸⁴ and ggplot⁸⁵ packages from R. The open access license can be found at <https://www.r-project.org/Licenses>. In all the batch tests, unpaired two-sided Student's *t*-tests were used to detect significant differences between the experimental groups and control groups. Linear correlation among gene abundance in global CA was calculated using parametric Pearson correlation. All experiments were performed with at least three biologically independent replicates. Data are presented as mean ± SD.

Reporting summary

Further information on research design is available in the Nature Portfolio Reporting Summary linked to this article.

Data availability

All raw metagenomes and metatranscriptomes were deposited to the NCBI Sequence Read Archive under the BioProject accession number PRJNA900728 [<https://www.ncbi.nlm.nih.gov/bioproject/?term=900728>]. Sequence Read Archive and corresponding hyperlink of the global metagenomic sample of CA were summarized in Supplementary Data 2. Raw metagenome data from the Tara Oceans global dataset PRJEB1787 [<https://www.ncbi.nlm.nih.gov/bioproject/196960>] were downloaded from the European Nucleotide Archive and were summarized in Supplementary Data 5. Source data are provided as a Source Data file. Source data are provided with this paper.

References

- Tian, F., Toon, O. B., Pavlov, A. A. & De Sterck, H. A Hydrogen-rich early Earth atmosphere. *Science* **308**, 1014–1017 (2005).
- Moody, E. R. R. et al. The nature of the last universal common ancestor and its impact on the early Earth system. *Nat. Ecol. Evol.* **8**, 1654–1666 (2024).
- Lappan, R. et al. Molecular hydrogen in seawater supports growth of diverse marine bacteria. *Nat. Microbiol.* **8**, 581–595 (2023).
- Ruff, S. E. et al. Hydrogen and dark oxygen drive microbial productivity in diverse groundwater ecosystems. *Nat. Commun.* **14**, 3194 (2023).
- Strohm, T. O., Griffin, B., Zumft, W. G. & Schink, B. Growth yields in bacterial denitrification and nitrate ammonification. *Appl. Environ. Microbiol.* **73**, 1420–1424 (2007).
- Hutchins, D. A. & Capone, D. G. The marine nitrogen cycle: new developments and global change. *Nat. Rev. Microbiol.* **20**, 401–414 (2022).
- Bianchi, D., Weber, T. S., Kiko, R. & Deutsch, C. Global niche of marine anaerobic metabolisms expanded by particle micro-environments. *Nat. Geosci.* **11**, 263–268 (2018).
- Wang, W. L., Moore, J. K., Martiny, A. C. & Primeau, F. W. Convergent estimates of marine nitrogen fixation. *Nature* **566**, 205–211 (2019).
- Stams, A. J. M. & Plugge, C. M. Electron transfer in syntrophic communities of anaerobic bacteria and archaea. *Nat. Rev. Microbiol.* **7**, 568–577 (2009).
- Carrier, D., Wawrousek, K., Eckert, C., Yu, J. & Maness, P.-C. The role of the bidirectional hydrogenase in cyanobacteria. *Bioresour. Technol.* **102**, 8368–8377 (2011).
- Moore, R. M., Punshon, S., Mahaffey, C. & Karl, D. The relationship between dissolved hydrogen and nitrogen fixation in ocean waters. *Deep Sea Res. Part I Oceanogr. Res. Pap.* **56**, 1449–1458 (2009).
- Vincent, K. A. et al. Electrochemical definitions of O₂ sensitivity and oxidative inactivation in hydrogenases. *J. Am. Chem. Soc.* **127**, 18179–18189 (2005).
- Eichner, M., Basu, S., Gledhill, M., de Beer, D. & Shaked, Y. Hydrogen dynamics in trichodesmium colonies and their potential role in mineral iron acquisition. *Front. Microbiol.* **10**, 01565 (2019).
- Nielsen, M., Revsbech, N. P. & Kühl, M. Microsensor measurements of hydrogen gas dynamics in cyanobacterial microbial mats. *Front. Microbiol.* **6**, 00726 (2015).
- Burow, L. C. et al. Hydrogen production in photosynthetic microbial mats in the Elkhorn Slough estuary, Monterey Bay. *ISME J.* **6**, 863–874 (2012).
- Hoehler, T. M., Bebout, B. M. & Des Marais, D. J. The role of microbial mats in the production of reduced gases on the early Earth. *Nature* **412**, 324–327 (2001).
- Murakami, T. et al. Metagenomics reveals global-scale contrasts in nitrogen cycling and cyanobacterial light-harvesting mechanisms in glacier cryoconite. *Microbiome* **10**, 50 (2022).
- Pfreundt, U. et al. Controlled motility in the cyanobacterium Trichodesmium regulates aggregate architecture. *Science* **380**, 830–835 (2023).
- Allredge, A. L. & Silver, M. W. Characteristics, dynamics and significance of marine snow. *Prog. Oceanogr.* **20**, 41–82 (1988).
- Tschitschko, B. et al. Rhizobia–diatom symbiosis fixes missing nitrogen in the ocean. *Nature* **630**, 899–904 (2024).
- Burow, L. C. et al. Identification of desulfobacterales as primary hydrogenotrophs in a complex microbial mat community. *Geobiology* **12**, 221–230 (2014).
- Wong, H. L. et al. Disentangling the drivers of functional complexity at the metagenomic level in Shark Bay microbial mat microbiomes. *ISME J.* **12**, 2619–2639 (2018).
- Trebuch, L. M. et al. High resolution functional analysis and community structure of photogranules. *ISME J.* **17**, 870–879 (2023).
- Cao, J. et al. Correlations of nitrogen removal and core functional genera in full-scale wastewater treatment plants: influences of different treatment processes and influent characteristics. *Bioresour. Technol.* **297**, 122455 (2020).
- Greening, C. et al. Genomic and metagenomic surveys of hydrogenase distribution indicate H₂ is a widely utilised energy source for microbial growth and survival. *ISME J.* **10**, 761–777 (2016).
- McIntosh, C. L., Germer, F., Schulz, R., Appel, J. & Jones, A. K. The [NiFe]-hydrogenase of the cyanobacterium synechocystis sp. PCC

- 6803 works bidirectionally with a bias to H₂ production. *J. Am. Chem. Soc.* **133**, 11308–11319 (2011).
27. Kessler, A. J. et al. Bacterial fermentation and respiration processes are uncoupled in anoxic permeable sediments. *Nat. Microbiol.* **4**, 1014–1023 (2019).
 28. Bourke, M. F. et al. Metabolism in anoxic permeable sediments is dominated by eukaryotic dark fermentation. *Nat. Geosci.* **10**, 30–35 (2017).
 29. Ji, B., Zhang, M., Gu, J., Ma, Y. & Liu, Y. A self-sustaining synergetic microalgal-bacterial granular sludge process towards energy-efficient and environmentally sustainable municipal wastewater treatment. *Water Res.* **179**, 115884 (2020).
 30. Marshall, I. P. G. et al. The hydrogenase chip: a tiling oligonucleotide DNA microarray technique for characterizing hydrogen-producing and -consuming microbes in microbial communities. *ISME J.* **6**, 814–826 (2012).
 31. Duffner, C. et al. Genotypic and phenotypic characterization of hydrogenotrophic denitrifiers. *Environ. Microbiol.* **24**, 1887–1901 (2022).
 32. Duffner, C. et al. Dechloromonas and close relatives prevail during hydrogenotrophic denitrification in stimulated microcosms with oxic aquifer material. *FEMS Microbiol. Ecol.* **97**, fiab004 (2021).
 33. Xiong, W. et al. Silicification-induced cell aggregation for the sustainable production of H₂ under aerobic conditions. *Angew. Chem. Int. Ed.* **54**, 11961–11965 (2015).
 34. Baebprasert, W., Jantaro, S., Khetkorn, W., Lindblad, P. & Incharoensakdi, A. Increased H₂ production in the cyanobacterium *Synechocystis* sp. strain PCC 6803 by redirecting the electron supply via genetic engineering of the nitrate assimilation pathway. *Metab. Eng.* **13**, 610–616 (2011).
 35. Ohmori, M., Ohmori, K. & Strotmann, H. Inhibition of nitrate uptake by ammonia in a blue-green alga, *Anabaena cylindrica*. *Arch. Microbiol.* **114**, 225–229 (1977).
 36. Trembath-Reichert, E., Butterfield, D. A. & Huber, J. A. Active subsurface microbial communities from Mariana back-arc venting fluids share metabolic strategies across different thermal niches and taxa. *ISME J.* **13**, 2264–2279 (2019).
 37. McAllister, S. M., Vandzura, R., Keffer, J. L., Polson, S. W. & Chan, C. S. Aerobic and anaerobic iron oxidizers together drive denitrification and carbon cycling at marine iron-rich hydrothermal vents. *ISME J.* **15**, 1271–1286 (2020).
 38. Karanasios, K. A., Vasiladiou, I. A., Pavlou, S. & Vayenas, D. V. Hydrogenotrophic denitrification of potable water: a review. *J. Hazard. Mater.* **180**, 20–37 (2010).
 39. Beaulieu, J. J., DelSontro, T. & Downing, J. A. Eutrophication will increase methane emissions from lakes and impoundments during the 21st century. *Nat. Commun.* **10**, 1375 (2019).
 40. Li, P. et al. Nitrogen removal and N₂O accumulation during hydrogenotrophic denitrification: influence of environmental factors and microbial community characteristics. *Environ. Sci. Technol.* **51**, 870–879 (2017).
 41. Kossalbayev, B. D. et al. Biotechnological production of hydrogen: design features of photobioreactors and improvement of conditions for cultivating cyanobacteria. *Int. J. Hydrog. Energy* **49**, 413–432 (2024).
 42. Canfield, D. E., Glazer, A. N. & Falkowski, P. G. The evolution and future of Earth's nitrogen cycle. *Science* **330**, 192–196 (2010).
 43. Wu, Z. et al. Imbalance of global nutrient cycles exacerbated by the greater retention of phosphorus over nitrogen in lakes. *Nat. Geosci.* **15**, 464–468 (2022).
 44. Huang, Y., Chen, X. & Ostrovsky, I. CyanoBACTERIAL BLOOMS ENHANCE NITROGEN REMOVAL IN LAKES THROUGH CARBON/NITROGEN COUPLING METabolism. *ACS EST Water* **3**, 3244–3252 (2023).
 45. Greening, C., Islam, Z. F. & Bay, S. K. Hydrogen is a major lifeline for aerobic bacteria. *Trends Microbiol.* **30**, 330–337 (2022).
 46. Devol, A. H. Denitrification, anammox, and n₂ production in marine sediments. *Annu. Rev. Mar. Sci.* **7**, 403–423 (2015).
 47. Berghuis, B. A. et al. Hydrogenotrophic methanogenesis in archaeal phylum Verstraetearchaeota reveals the shared ancestry of all methanogens. *Proc. Natl. Acad. Sci. USA* **116**, 5037–5044 (2019).
 48. Hodgskiss, M. S. W., Crockford, P. W., Peng, Y., Wing, B. A. & Horner, T. J. A productivity collapse to end Earth's great oxidation. *Proc. Natl. Acad. Sci. USA* **116**, 17207–17212 (2019).
 49. Martinez-Gutierrez, C. A., Uyeda, J. C. & Aylward, F. O. A timeline of bacterial and archaeal diversification in the ocean. *eLife* **12**, RP88268 (2023).
 50. Klawonn, I., Bonaglia, S., Bruchert, V. & Ploug, H. Aerobic and anaerobic nitrogen transformation processes in N₂-fixing cyanobacterial aggregates. *ISME J.* **9**, 1456–1466 (2015).
 51. Islam, Z. F. et al. Two Chloroflexi classes independently evolved the ability to persist on atmospheric hydrogen and carbon monoxide. *ISME J.* **13**, 1801–1813 (2019).
 52. Kong, L. et al. Cross-feeding between filamentous cyanobacteria and symbiotic bacteria favors rapid photogranulation. *Environ. Sci. Technol.* **57**, 16953–16963 (2023).
 53. Alattabi, A. W. et al. An investigation into the effect of MLSS on the effluent quality and sludge settleability in an aerobic-anoxic sequencing batch reactor (AASBR). *J. Water Process. Eng.* **30**, 100479 (2019).
 54. Schneider, C. A., Rasband, W. S. & Eliceiri, K. W. NIH image to imageJ: 25 years of image analysis. *Nat. Methods* **9**, 671–675 (2012).
 55. Abouhend, A. S. et al. Growth progression of oxygenic photogranules and its impact on bioactivity for aeration-free wastewater treatment. *Environ. Sci. Technol.* **54**, 486–496 (2020).
 56. Wei, S. et al. Partitioning of nutrient removal contribution between granules and flocs in a hybrid granular activated sludge system. *Water Res.* **203**, 117514 (2021).
 57. Bédard, C. & Knowles, R. Physiology, biochemistry, and specific inhibitors of CH₄, NH₄⁺, and CO oxidation by methanotrophs and nitrifiers. *Microbiol. Rev.* **53**, 68–84 (1989).
 58. Krustok, I., Odlare, M., Truu, J. & Nehrenheim, E. Inhibition of nitrification in municipal wastewater-treating photobioreactors: effect on algal growth and nutrient uptake. *Bioresour. Technol.* **202**, 238–243 (2016).
 59. Burow, L. C. et al. Anoxic carbon flux in photosynthetic microbial mats as revealed by metatranscriptomics. *ISME J.* **7**, 817–829 (2012).
 60. Prensner, J. R. et al. Transcriptome sequencing across a prostate cancer cohort identifies PCAT-1, an unannotated lincRNA implicated in disease progression. *Nat. Biotechnol.* **29**, 742–749 (2011).
 61. Feng, Y. et al. Discrepant gene functional potential and cross-feedings of anammox bacteria *Ca. Jettenia caeni* and *Ca. Brocadia sinica* in response to acetate. *Water Res.* **165**, 114974 (2019).
 62. Peng, Y. et al. IDBA-UD: a de novo assembler for single-cell and metagenomic sequencing data with highly uneven depth. **28**, 1420–1428 (2012).
 63. Bushnell, B. *BBMap: A Fast, Accurate, Splice-Aware Aligner*. (Lawrence Berkeley National Laboratory, Berkeley, CA, United States, 2014).
 64. Menzel, P., Ng, K. L. & Krogh, A. Fast and sensitive taxonomic classification for metagenomics with Kaiju. *Nat. Commun.* **7**, 11257 (2016).
 65. Darling, A. et al. PhyloSift: phylogenetic analysis of genomes and metagenomes. *PeerJ* **2**, e243 (2014).
 66. Katoh, K., Misawa, K., Kuma, K. & Miyata, T. MAFFT: a novel method for rapid multiple sequence alignment based on fast Fourier transform. *Nucleic Acids Res.* **30**, 3059–3066 (2002).
 67. Olm, M. R., Brown, C. T., Brooks, B. & Banfield, J. F. dRep: a tool for fast and accurate genomic comparisons that enables improved

- genome recovery from metagenomes through de-replication. *ISME J.* **11**, 2864–2868 (2017).
68. Tong, F. et al. The microbiome of the buffalo digestive tract. *Nat. Commun.* **13**, 823 (2022).
 69. Chaumeil, P.-A., Mussig, A. J., Hugenholtz, P. & Parks, D. H. GTDB-Tk: a toolkit to classify genomes with the Genome Taxonomy Database. *Bioinformatics* **36**, 1925–1927 (2019).
 70. Zhou, Z. et al. METABOLIC: high-throughput profiling of microbial genomes for functional traits, metabolism, biogeochemistry, and community-scale functional networks. *Microbiome* **10**, 33 (2022).
 71. Buchfink, B., Xie, C. & Huson, D. H. Fast and sensitive protein alignment using DIAMOND. *Nat. Methods* **12**, 59–60 (2015).
 72. Anders, S., Pyl, P. T. & Huber, W. HTSeq—a Python framework to work with high-throughput sequencing data. *Bioinformatics* **31**, 166–169 (2015).
 73. Wagner, G. P., Kin, K. & Lynch, V. J. Measurement of mRNA abundance using RNA-seq data: RPKM measure is inconsistent among samples. *Theory Biosci.* **131**, 281–285 (2012).
 74. Kalyaanamoorthy, S., Minh, B. Q., Wong, T. K. F., von Haeseler, A. & Jermini, L. S. ModelFinder: fast model selection for accurate phylogenetic estimates. *Nat. Methods* **14**, 587–589 (2017).
 75. Nguyen, L.-T., Schmidt, H. A., von Haeseler, A. & Minh, B. Q. IQ-TREE: a fast and effective stochastic algorithm for estimating maximum-likelihood phylogenies. *Mol. Biol. Evol.* **32**, 268v274 (2014).
 76. Dohrmann, A. B. & Krüger, M. Microbial H₂ consumption by a formation fluid from a natural gas field at high-pressure conditions relevant for underground H₂ storage. *Environ. Sci. Technol.* **57**, 1092–1102 (2023).
 77. Broecker, W. S. & Peng, T.-H. Gas exchange rates between air and sea. *Tellus* **26**, 21–35 (1974).
 78. Suárez-Ojeda, M. E. et al. Characterization of a p-nitrophenol-degrading mixed culture with an improved methodology of fluorescence in situ hybridization and confocal laser scanning microscopy. *J. Chem. Technol. Biotechnol.* **86**, 1405–1412 (2011).
 79. Almeida, J. R., Fradinho, J. C., Carvalho, G., Oehmen, A. & Reis, M. A. M. Dynamics of microbial communities in phototrophic polyhydroxyalkanoate accumulating cultures. *Microorganisms* **10**, 351 (2022).
 80. Albuquerque, M. G. E., Torres, C. A. V. & Reis, M. A. M. Polyhydroxyalkanoate (PHA) production by a mixed microbial culture using sugar molasses: effect of the influent substrate concentration on culture selection. *Water Res.* **44**, 3419–3433 (2010).
 81. dos Reis, M. & Yang, Z. Approximate likelihood calculation on a phylogeny for bayesian estimation of divergence times. *Mol. Biol. Evol.* **28**, 2161–2172 (2011).
 82. Lee, M. D. GToTree: a user-friendly workflow for phylogenomics. *Bioinformatics* **35**, 4162–4164 (2019).
 83. Zhao, R., Zhang, I. H., Jayakumar, A., Ward, B. B. & Babbitt, A. R. Age, metabolisms, and potential origin of dominant anammox bacteria in the global oxygen-deficient zones. *ISME Commun.* **4**, ycae060 (2024).
 84. Pebesma, E. Simple features for R: standardized support for spatial vector data. *R. J.* <https://doi.org/10.32614/RJ-2018-009> (2018).
 85. Wickham, H. *ggplot2: Elegant Graphics for Data Analysis* (Springer New York, 2016).

Acknowledgements

This work was supported by the National Key Research and Development Program of China, Grant No. 2022YFC3203003 (S.T.L.) and National Natural Science Foundations of China, Grant No. 52270016 (S.T.L.) and 523B2095 (L.R.K.).

Author contributions

L.K. and S.L. conceived the idea and designed the experiments. L.K., Y.F., and R.Z. performed the experiments. L.K., J.S., X.W., and Y.M. analyzed the data. L.K., S.L., and X.W. wrote and revised the manuscript. All the authors contributed to the interpretation of the data and preparation of the manuscript.

Competing interests

The authors declare no competing interests.

Additional information

Supplementary information The online version contains supplementary material available at <https://doi.org/10.1038/s41467-025-60327-x>.

Correspondence and requests for materials should be addressed to Sitong Liu.

Peer review information *Nature Communications* thanks Joanne Boden, Weiwei Cai, Chris Greening, and the other, anonymous, reviewer(s) for their contribution to the peer review of this work. A peer review file is available.

Reprints and permissions information is available at <http://www.nature.com/reprints>

Publisher's note Springer Nature remains neutral with regard to jurisdictional claims in published maps and institutional affiliations.

Open Access This article is licensed under a Creative Commons Attribution-NonCommercial-NoDerivatives 4.0 International License, which permits any non-commercial use, sharing, distribution and reproduction in any medium or format, as long as you give appropriate credit to the original author(s) and the source, provide a link to the Creative Commons licence, and indicate if you modified the licensed material. You do not have permission under this licence to share adapted material derived from this article or parts of it. The images or other third party material in this article are included in the article's Creative Commons licence, unless indicated otherwise in a credit line to the material. If material is not included in the article's Creative Commons licence and your intended use is not permitted by statutory regulation or exceeds the permitted use, you will need to obtain permission directly from the copyright holder. To view a copy of this licence, visit <http://creativecommons.org/licenses/by-nc-nd/4.0/>.

© The Author(s) 2025